JOURNAL OF SYNCHROTRON RADIATION
ISSN 1600-5775

Electronic structure variations of polar and nonpolar ZnO lattices with nitrogen-ion bombardment using synchrotron-based *in situ* photoemission and X-ray absorption spectroscopy

Yuyang Huang,[a] Yaping Li,[a,b]* Meng Wu,[a]* Hui-Qiong Wang,[a,c]* Xuebin Yuan,[a] Turghunjan Gholam,[a] Hui Zeng,[a] Jia-Ou Wang,[d] Rui Wu,[d] Hai-Jie Qian,[d] Yufeng Zhang[a] and Junyong Kang[a]

[a]Fujian Provincial Key Laboratory of Semiconductors and Applications, Collaborative Innovation Center for Optoelectronic Semiconductors and Efficient Devices, Department of Physics, Xiamen University, Xiamen 361005, People's Republic of China, [b]College of Science, Henan University of Technology, Zhengzhou 450001, People's Republic of China, [c]Xiamen University Malaysia, Sepang, Selangor 439000, Malaysia, and [d]Beijing Synchrotron Radiation Facility, Institute of High Energy Physics, Chinese Academy of Sciences, Beijing 100049, People's Republic of China. *Correspondence e-mail: 374206971@qq.com, meng.wu@xmu.edu.cn, hqwang@xmu.edu.cn

Received 2 July 2019
Accepted 10 October 2019

Edited by K. Kvashnina, ESRF – The European Synchrotron, France

Keywords: polar and nonpolar; nitrogen-ion bombardment; electronic structures.

Surface polarity with different crystal orientations has been demonstrated as a crucial parameter in determining the physical properties and device applications in many transition metal oxide and semiconductor compound systems. The influences of surface polarity on electronic structures in nitrogen-incorporated ZnO lattices have been investigated in the present work. The successful doping of nitrogen atoms in ZnO lattices is suggested by the existence of N-related chemical bonds obtained from X-ray photoelectron spectroscopy analysis where a pronounced N–Zn peak intensity has been observed in the $(000\bar{1})$-terminated polar ZnO compound compared with the $(10\bar{1}0)$-terminated nonpolar ZnO compound. An energy shift of the valence band maximum towards the Fermi level has been resolved for both polar and nonpolar ZnO lattices, whereas a charge redistribution of the O 2*p* hybridized states is only resolved for *o*-plane ZnO with a polar surface. Angular-dependent X-ray absorption analyses at the O *K*-edge reveal enhanced surface-state contributions and asymmetric O 2*p* orbital occupations in the $(000\bar{1})$-terminated *o*-plane ZnO compound. The results shed light on the efficient nitrogen doping in ZnO lattices with polar surfaces. The comprehensive electronic structure investigations of correlations between impurity doping and surface polarity in ZnO lattices may also offer guidance for the material design in other transition metal oxide and semiconductor systems.

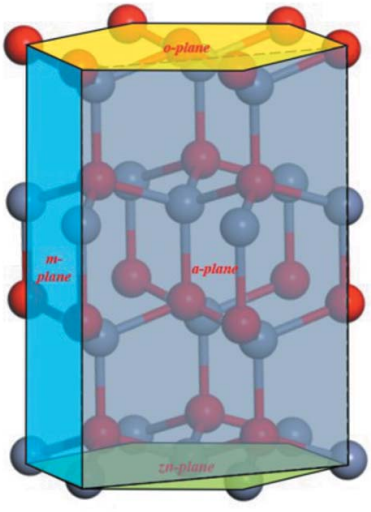

1. Introduction

As an appropriate optoelectronic material for short-wavelength light-emitting diodes (LEDs) and laser diodes, ZnO has received close attention for decades. The most attractive characteristics of ZnO-based materials is the direct band gap of 3.37 eV enabling optoelectronics applications in the blue or UV region and, moreover, a large exciton binding energy of 60 meV at room temperature, showing potential applications for optical devices based on excitonic effects (Brillson *et al.*, 2013; Özgür *et al.*, 2005; Ogale, 2005; Nickel & Terukov, 2005; Lafrentz *et al.*, 2013). To realize these applications, high-quality pn junctions based on ZnO materials need to be achieved; therefore, fabricating stable p-type ZnO is an imperative step. Unfortunately, ZnO faces the long-standing doping asymmetry problem, which means as-grown ZnO films showing an intrinsic n-type conductivity are formed in most

cases, and p-type features are difficult to achieve by doping or other methods. This phenomenon could be partly due to its self-compensation caused by intrinsic defects which are an extreme hinderance to the development of ZnO-based optoelectronic devices (Fan *et al.*, 2013). Different doping elements and synthesis methods have been employed to overcome this barrier, among which nitrogen is a promising acceptor impurity, not only because of its similar atomic size but also the comparable on-site energy of the 2*p* valence state with respect to the O 2*p* states (Janotti & Walle, 2009). Hence a profusion of studies focused on this theme have tried to produce stable p-type N-doped ZnO systems. However, low solubility of nitrogen and unexpected deep-level defects such as $(N_2)O$, which are not beneficial for p-type formation, are observed (Fan *et al.*, 2013). Thus, more efforts are required to reveal the underlying mechanism regarding nitrogen incorporation in ZnO lattices.

From a crystallography point of view, wurtzite ZnO shares the most stable structure which can be divided into two categories depending on polarity. The polar surfaces are cleaved perpendicular to the *c* axis, showing a spontaneous polarization, which can be either a (0001)-terminated Zn-plane or a $(000\bar{1})$-terminated *o*-plane since the atomic structure of ZnO along the crystal *c* axis is composed of alternative atomic layers of Zn and O atoms. Moreover, the nonpolar surfaces are defined by cleaved directions parallel to the crystal *c* axis, *i.e.* the $(10\bar{1}0)$-terminated *m*-plane or the $(11\bar{2}0)$-terminated *a* plane, as illustrated in Fig. 1(*a*). The different atomic crystal structures for polar and nonpolar ZnO in terms of various bond lengths and symmetries as well as the intrinsic built-in electric field existing only for polar ZnO induce significant influences on the physical properties and device applications. For instance, the electronic conductivity (Maki *et al.*, 2003), the incorporation of impurities (Li *et al.*, 2000) and the thin-film deposition conditions (Zhou *et al.*, 2012) have been shown experimentally to have a strong dependence on the surface polarity, which are further addressed by theoretical calculations (Wang *et al.*, 2005; Gasset *et al.*, 1991; Allen *et al.*, 2009; Yang *et al.*, 2009; Williams *et al.*, 2011). However, a comprehensive understanding of the electronic structure variations upon doping with different surface polarity is still lacking, which will be addressed in the present work using synchrotron-based frontier spectroscopic techniques.

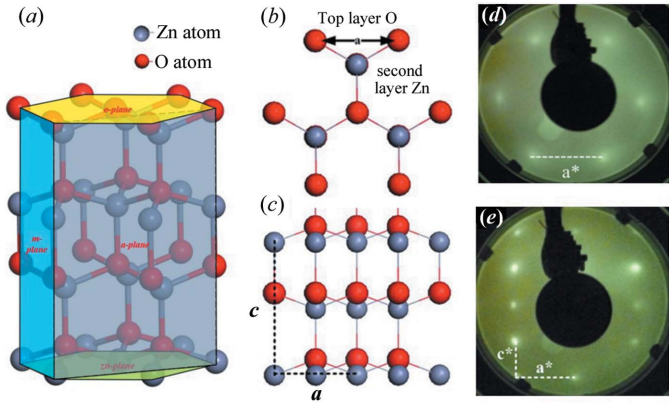

Figure 1
(*a*) Schematic view of the ZnO wurtzite structure with different crystal orientations. (*b*) and (*c*) Specific *o*-plane and *m*-plane atomic structures. LEED diffraction patterns of the (*d*) *o*-plane and (*e*) *m*-plane ZnO.

In this article, we aim to provide detailed electronic structure studies on nitrogen-incorporated ZnO lattices, including both the $(000\bar{1})$-terminated polar *o*-plane and the $(10\bar{1}0)$-terminated nonpolar *m*-plane ZnO surfaces. The N-ion bombardment method has been utilized to induce dopants in ZnO lattices. After N-ion bombardment, *in situ* X-ray photoelectron spectroscopy (XPS) measurements were performed to determine the chemical bonding information which confirms the existence of N-related bonds. The variations of the electronic states of conduction bands near the Fermi level have been investigated by UV photoelectron spectroscopy (UPS), where both energy shifts of the valence band maximum (VBM) towards the Fermi level and the charge redistribution of the O 2*p* hybridized states have been resolved. Furthermore, angular-dependent X-ray absorption spectroscopy (XAS) measurements at the O *K*-edge are used to determine the conduction band information near the Fermi level. In comparison with the N-doped polar and nonpolar ZnO lattices, the variations of the electronic structure upon nitrogen incorporation suggest a more favorable chemical environment for efficient doping of N atoms into *o*-plane ZnO lattices, as will be discussed in the main text. Our results offer a detailed understanding on the modification of the electronic structure toward p-type doping of ZnO and may offer guidance for material design in other similar systems with both polar and nonpolar interfaces.

2. Experimental details

ZnO single crystals with different *o*-plane $(000\bar{1})$-terminated and *m*-plane $(10\bar{1}0)$-terminated orientations with dimensions of 10 mm × 10 mm × 1 mm, purchased directly from Hefei Kejing Materials Technology Co. Ltd, were utilized for N-ion bombardment and further spectroscopy characterizations. Before N-ion bombardment, ZnO samples were first cleaned in ethyl alcohol through an ultrasonic cleaning process and heated in a vacuum system (1.1×10^{-9} Torr) at 600°C to remove contained gases for 1 h. After that the samples were bombarded with 1 kV Ar^+ ions for 30 min, followed by annealing at 600°C for 1 h to fabricate surfaces with low contaminations. Subsequently, *in situ* low-energy electron diffraction (LEED) measurements were performed with a beam energy between 50 eV and 130 eV at a close-to-normal electron incident angle to identify the crystal orientations. Ion bombardment was carried out using N^{2+} ions with a kinetic energy of 5 keV and a target current of about 1.8 µA for 30 min at room temperature for *m*-plane and *o*-plane ZnO.

After N-ion bombardment, *in situ* XPS, UPS and XAS spectra were collected at the Beijing Synchrotron Radiation Facility (4B9B beamline) to characterize the local electronic structures of ZnO lattices where the ultra-high-vacuum system shows a basic pressure of better than 5×10^{-9} Torr. *In situ* XPS and UPS were carried out at an incident angle of 6.75°

(normal detection) with respective incoming beam energies of 720 eV and 36 eV. Furthermore, *in situ* XAS spectra with linearly polarized light (horizontal polarization ~80%) were collected using the total electron yield (TEY) mode. The N *K*-edge along with the angular-dependent O *K*-edge XAS measurements were recorded with an energy step width of 0.1 eV. The energy shifts of all spectra were calibrated by setting the measured Au *4f* 7/2 binding energies to 83.80 ± 0.05 eV with regard to the Fermi energy. The instrument work function was included in the data processing. All the aforementioned experiments were performed at the 4B9B beamline of the Beijing Synchrotron Radiation Facility (BSRF).

3. Results and discussion

After Ar^+-ion bombardment of the ZnO surfaces, *in situ* surface-sensitive LEED measurements were performed to determine the crystal structure where a detailed analysis of the diffraction spot positions yields information of the surface crystal symmetry. The identical ZnO wurtzite structure of different crystal orientations is plotted in Fig. 1(*a*), where the specific *o*-plane and *m*-plane atomic structures are shown in Figs. 1(*b*) and 1(*c*), respectively. Figs. 1(*d*) and 1(*e*) exhibit the LEED patterns of ZnO surfaces after Ar^+-ion etching and the subsequent annealing procedure. The absence of an additional superstructure has been observed for both polar and nonpolar ZnO samples, confirming that their surface orientations are, as expected, $(000\bar{1})$-terminated and $(10\bar{1}0)$-terminated, respectively.

The LEED diffraction pattern shown on the fluorescence screen exhibits a hexagonal symmetry as recorded in Fig. 1(*d*) for *o*-plane ZnO, suggesting a similar hexagonal symmetry for the real-space structure. The resolved hexagonal symmetry is consistent with the ideal top-layer structure for the ZnO $(000\bar{1})$ (1×1) orientation, as compared with the theoretical structure model illustrated in Fig. 1(*b*) formed by pure O atoms of the top layer. Fig. 1(*e*) exhibits the LEED diffraction spots of *m*-plane ZnO which shows a rectangular symmetry with $c^*/a^* \simeq 0.6$. The real-space structure thus can be constructed with the same rectangular symmetry but stretches in the opposite manner following the reciprocal dependence of the lattice structure, *i.e.* the real-space lattice constant ratio $a/c \simeq 0.6$. The rectangular surface structural symmetry and the a/c value are approximately the same as the theoretical structural pattern as shown in Fig. 1(*c*), revealing the particular structure of nonpolar *m*-plane ZnO (Jedrecy *et al.*, 2000).

For the purpose of determining the chemical bonding and the electronic structures of the investigated samples, XPS measurements have been carried out for *o*-plane ZnO and *m*-plane ZnO before and after nitrogen incorporation. Fig. 2(*a*) shows the survey scans with binding energies up to 550 eV, where representative excitation peaks similar to those of the ZnO wurtzite structure have been observed, *i.e.* O 1*s*, O 2*s*, Zn 3*s*, Zn 3*p* and Zn 3*d* peaks located at binding energies of 530.5, 25, 140, 90 and 10 eV, respectively (Lashkarev *et al.*, 2015). For the XPS measurements at the O 1*s* and N 1*s* edges, the excited kinetic energy is about 200–300 eV for an incident photon

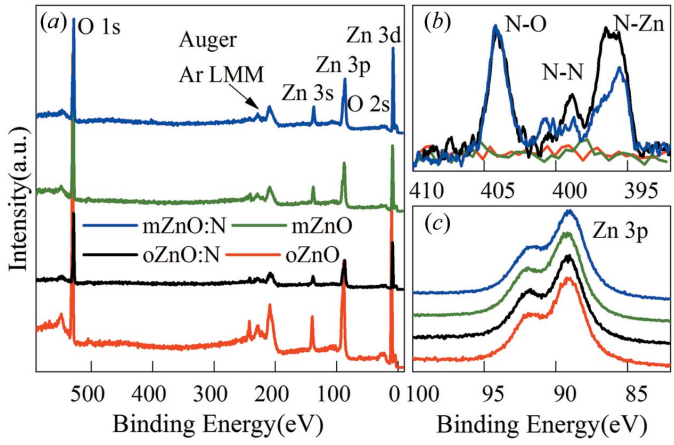

Figure 2
(*a*) Evolution of the survey scans for, from top to bottom, $(10\bar{1}0)$-terminated *m*-plane ZnO after nitrogen doping, pristine *m*-plane ZnO, $(000\bar{1})$-terminated *o*-plane ZnO after nitrogen doping, and pristine *o*-plane ZnO. N 1*s* and Zn 3*p* core-level XPS spectra of different orientations (*b*) after and (*c*) before nitrogen doping.

energy of 720 eV, and the mean free path λ is about 4 nm as suggested from the 'universal curve' for the inelastic mean free path (Seah & Dench, 1979). The probe depth is approximately 12 nm.

Fig. 2(*b*) depicts the fine core-level XPS scans at the N 1*s* absorption edge in the energy range 390–410 eV. The nitrogen-incorporated nonpolar *m*-plane ZnO and polar *o*-plane ZnO samples show characteristic N-related excitation peaks. The N 1*s* spectra contain mainly three components, which can be further assigned to different chemical bonds of nitrogen with its surrounding atoms. The lower-energy component at ~397 eV corresponds to Zn—N bond formation, whereas the higher-energy component at about 404 eV is caused by the appearance of N—O bonds (Lashkarev *et al.*, 2015; Petravic *et al.*, 2006; Bian *et al.*, 2004). The existence of the N—Zn and N—O excitation peaks indicates the successful doping of nitrogen atoms in ZnO lattices, where the formation of the desired N—Zn bonds can be considered as one of the essential ingredients for p-type doping in the ZnO compound. The weak intensity peak located at about 400 eV can be attributed to the N—N chemical bond as reported in the literature (Rochet, 1998), revealing the existence of molecular nitrogen arising from the N_2 absorbed near the surface. We note that there is no clear N-related peak at the N 1*s* edge for pristine ZnO samples before N-ion bombardment with the same Ar^+ ion etching and post-annealing treatments [the green and red curves in Fig. 2(*b*)], suggesting that the N-related signals are mainly related to the incorporation of N ions rather than the N-ion adsorption at the sample surfaces. In addition, compared with the influence of nitrogen doping on different orientation terminated ZnO single crystals, we notice that a stronger N—Zn peak intensity exists for the *o*-plane polar surface than for the nonpolar case. This is similar to the result suggested by first-principle calculations, where the formation energy for N substituting Zn in the O-rich surface is lower than that of the Zn-rich surface (Wang *et al.*, 2016). The polar ZnO $(000\bar{1})$ with a surface full of O atoms thus may provide

a more favorable environment for nitrogen incorporation. Fig. 2(*c*) shows the normalized Zn 3*p* core-level XPS spectra for the polar ZnO $(000\bar{1})$ and nonpolar ZnO $(10\bar{1}0)$ as well as the corresponding doped films. No significant variation of the spectral lineshapes and the peak excitation energy has been observed in the Zn 3*p* core-level spectra, which conforms to former research findings that the binding energy of the Zn 3*p* core-level is independent of the change of chemical bonds in ZnO doping (Gao *et al.*, 2009).

The O 1*s* core-level XPS spectra of pristine nonpolar ZnO $(10\bar{1}0)$ and polar ZnO $(000\bar{1})$ as well as the corresponding nitrogen-incorporated samples are presented in Figs. 3(*a*) and 3(*c*), where all samples show a broad and asymmetric peak at ∼530.5 eV. For pristine ZnO samples, the O 1*s* XPS spectra contain double-peak structures. The high-intensity excitation peak located at ∼530.5 eV can be associated with intrinsic Zn—O bonds, whereas the peak located at ∼532.5 eV with a lower intensity can be attributed to the presence of loosely bound oxygen vacancies close to the surfaces (Chen *et al.*, 2000; Shinde *et al.*, 2012; Park *et al.*, 2006; Tabet *et al.*, 2008). The oxygen vacancy related excitation peaks present in pristine films may arise from Ar^+-ion bombardment or some intrinsic defects in ZnO single crystals (Janotti & Walle, 2009). After nitrogen doping, enhanced intensities of the high-energy excitation peak at ∼532.5 eV have been observed for both *o*-plane ZnO and *m*-plane ZnO samples, which will be discussed.

For a detailed understanding of the impact of nitrogen incorporation on different orientated ZnO lattices, the O 1*s* core-level XPS spectra are fitted by Lorentzian functions. Two chemical bonding states of O could be obtained after the spectra deconvolution: the high-energy feature located at ∼532.5 eV with spectral area labeled as A_1 and the low-energy feature located at ∼530.5 eV with spectral area labeled as A_2.

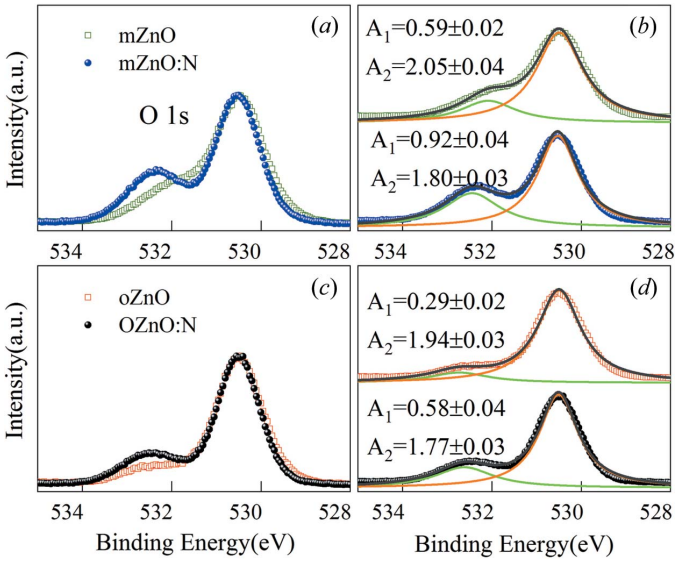

Figure 3
O 1*s* XPS core-level spectra of (*a*) the *m*-plane ZnO and (*c*) the *o*-plane ZnO lattices before and after N-ion bombardment. (*b*) and (*d*) Fitting curves of the XPS curves with two Lorentzian functions shown in (*a*) and (*c*), respectively. The spectral areas of the high- and low-energy excitation peaks are denoted as A_1 and A_2, respectively.

Table 1
Samples with different crystal orientations, the integrated peak areas of N 1*s* XPS spectra between 394 eV and 406 eV, the integrated peak areas of O 1*s* XPS spectra between 528 eV and 535 eV, and intensity ratios between N and O after cross-section correction.

Sample	Area N	Area O	Area N/Area O	Intensity ratio (%)
m-plane ZnO:N	2279.5	65434	0.035	5.2
o-plane ZnO:N	2187.0	76347	0.029	4.4

The intensity ratio A_1/A_2 reflects the relative proportion of each component. In comparison with the relative intensities of the two features (A_1/A_2) for all the investigated ZnO samples, we notice an obvious increase in the peak A_1 proportion after nitrogen incorporation, *i.e.* A_1/A_2 changes from ∼29% to 51% and from 15% to 32% for *m*-plane and *o*-plane ZnO before and after nitrogen doping, respectively. The increased percentage of peak A_1 can be ascribed to the increased amount of loosely bound oxygen vacancies due to high-energy N-ion bombardment. Moreover, there is a relatively larger proportion of A_1 for doped nonpolar *m*-plane ZnO compared with the *o*-plane ZnO. Given a comparable amount of oxygen vacancies created by N-ion bombardment due to the same experimental conditions, the more favorable environment for the occupation of O sites by N atoms for *o*-plane ZnO lattices compensates for the magnitude of oxygen vacancies. A small oxygen-deficient proportion is thus expected, which is consistent with the N 1*s* core-level spectra.

We further quantify the N concentration from the comparison of O 1*s* and N 1*s* intensities from the XPS spectra. After subtracting a linear background, we integrate the peak intensities of O 1*s* and N 1*s* XPS spectra, as shown in Table 1. The intensity ratios for N 1*s* and O 1*s* are 0.035 and 0.029 for *o*-plane ZnO:N and *m*-plane ZnO:N, respectively. To estimate the N concentration, the integrated peak area ratios are further corrected by the cross sections of N and O, *i.e.* the cross sections are about 0.2046 for N 1*s* and 0.3081 for O 1*s* at a photon energy of 700 eV (Yeh & Lindau, 1985). Assuming the N ions are homogeneously distributed in the layered ZnO structure, we obtain concentration ratios between N and O of approximately 5.2% and 4.4% for *m*-plane ZnO:N and *o*-plane ZnO:N, respectively. We note that these N doping concentrations are comparable with the results reported in the literature. Wei *et al.* reported nitrogen doping concentrations in ZnO which vary between 2.7% and 7.1% by changing the temperature and time of the NH_3 treatment based on XPS analyses (Wei *et al.*, 2005). The N concentration was 4.4% in another paper, where In is cooperatively doped to improve the concentration of N (Bian *et al.*, 2004).

In situ UPS measurements have been used to explore the variation of the electronic structure in the valence band upon nitrogen incorporation with an incoming photon energy of 36 eV. The main features of the UPS spectra are located between 1 eV and 13 eV as shown in Fig. 4. The strong peak located at ∼10.9 eV can be attributed to the excitations from Zn 3*d*. The multiplet structures between 3 eV and 9 eV are dominated by O 2*p* states hybridized with Zn 3*d* and Zn 4*s*

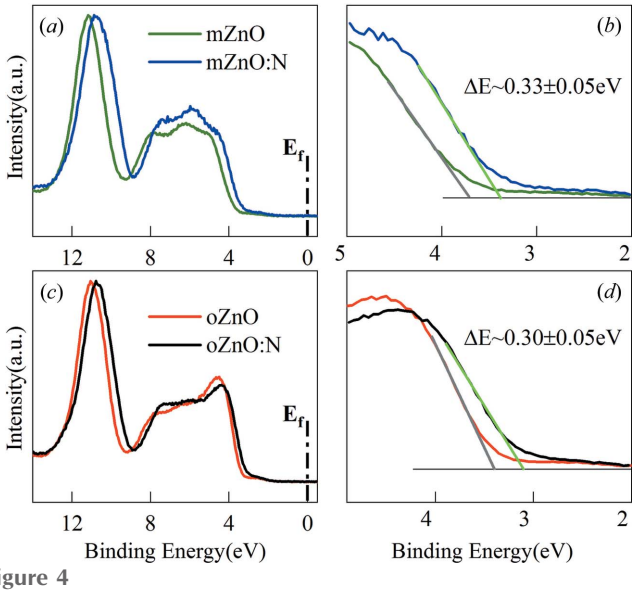

Figure 4
UPS spectra of nonpolar *m*-plane ZnO and polar *o*-plane lattices (*a*) before and (*c*) after N-ion bombardment. (*b*) and (*d*) Corresponding enlarged views near VBM with the fitted lines denoting the linear extrapolation of the UPS spectral edge.

energy levels (Perkins *et al.*, 2005). For pristine ZnO with various polarities, different peak intensities among the O 2*p* and O 2*p*–Zn 3*d*, O 2*p*–Zn 4*s* hybridized states can be observed which may be the result of the different bond distances and symmetries for different crystal orientations (Lin & Tsai, 2006). From the onset of the UPS spectra, the position of the VBM can be estimated by taking a linear extrapolation of the leading edge in the UPS spectra as shown in Figs. 4(*b*) and 4(*d*). The intersect of the fitting curve with respect to the extended base line corresponds to the energy difference between the VBM and the Fermi level. In comparison with the pristine and N-doped *m*-plane ZnO, the overall spectra retain the similar features but the VBM is shifted with $\Delta E \simeq 0.33 \pm 0.05$ eV towards the Fermi level. The binding energy shift shows a strong dependence on the chemical composition, *i.e.* the introduction of impurity defects (Guan *et al.*, 2008), the surface structure relaxation including the reduced coordination number of metal sites upon etching (Chang, 2004; Sun *et al.*, 2004) and the interfacial phenomena presented in heterojunctions, *etc.* (Zhang *et al.*, 2016). Our resolved energy shift of the VBM might relate to an acceptor defect as has been reported for many other N-doped ZnO systems (Kim *et al.*, 2010; Lin & Tsai, 2006), whereas the influence of surface-structure variations due to Ar^+ ion etching and the subsequent N-ion bombardment cannot be ruled out (Chang, 2004; Sun *et al.*, 2004). In order to reveal the influence of Ar^+ etching on the position of the VBM, we compare the values of the VBM of undoped ZnO samples with those in the literature, which are approximately 2.82 eV for a clean surface and 3.64 eV for a defect-induced surface (Kim *et al.*, 2010; Ghosh *et al.*, 2018). The energy difference of pristine ZnO in our measurement is about 3.3–3.5 eV. It reveals the influence of Ar^+ etching on the position of the VBM. Moreover, variations of both the spectral lineshape and the VBM edge are observed for *o*-plane ZnO before and after nitrogen incorporation. The change of the spectral lineshape implies a charge redistribution upon nitrogen doping, which reinforces that the $(000\bar{1})$-terminated polar surface is more favorable for the desired p-type doping as the newly formed N—Zn and N—O chemical bonds affect the original Zn—O hybridization, consistent with the results suggested by N 1*s* and O 1*s* core-level XPS spectra. The shift of the binding energy with respect to the Fermi level is about 0.30 ± 0.05 eV for N-doped *o*-plane ZnO, which is comparable with the value for *m*-plane ZnO within the experimental error bars.

Fig. 5 exhibits the N *K*-edge XANES spectra of N-doped ZnO surfaces with different *m*-plane and *o*-plane terminations, establishing a connection between the peak positions and the excitations from the initial N 1*s* state to the final N-related 2*p*-symmetry states. The spectra are characterized by a strong resonant peak at ~401 eV associated with the transition between the N 1*s* state and $2p\pi^*$ state, as reported previously for molecular nitrogen (Rochet, 1998). The appearance of the N 1*s*–π^* transition suggests that molecular nitrogen is formed in samples by N-ion bombardment, similar to the results obtained from N 1*s* XPS measurements. Accompanied by the replacement of O sites by N sites, different chemical bonds in the forms of N—Zn and N—O may be created in ZnO lattices, which in principle should be visible in N *K*-edge XAS spectra. A shoulder with a slightly higher photon energy appeared in the spectrum which can be attributed to the formation of different N—O chemical bonds in N-doped ZnO samples. For instance, this energy position is very close to the characteristic absorption peaks of molecular NO_2 at 403.2 eV and molecular N_2O at 404.7 eV (Schwarz *et al.*, 1977; Wight & Brion, 1974). However, the Zn—N chemical bonds reflecting the transition from N 1*s* to N 2*p* orbitals hybridized with transition metal sites are difficult to resolve due to the overlap of the excitation energies with the strong N_2-related resonance peak at ~401 eV, as has been previously reported for N-doped ZnO and in many other transition metal nitride systems (Chen, 2010; Petravic *et al.*, 2006).

Angular-dependent O *K*-edge absorption measurements have been performed to investigate the variation of electronic structures close to the Fermi level. O *K*-edge XAS spectra are

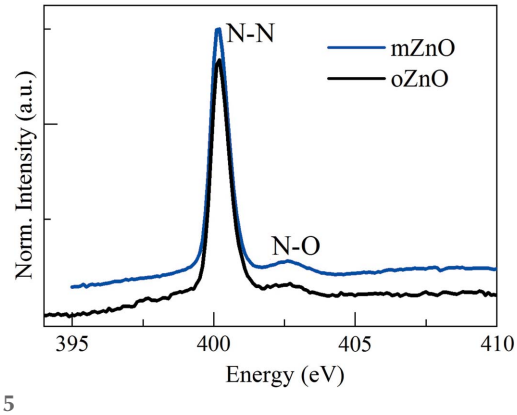

Figure 5
N *K*-edge XAS spectra of N-doped *m*-plane ZnO and *o*-plane ZnO lattices.

collected for $\theta = 90°$, 40° and 30° with θ denoting the angle between the incoming beam and the sample surface normal direction ($\theta = 90°$ corresponding to normal light incidence). A detailed angular-dependent measurement yields information about the projected density of states along in-plane and out-of-plane directions, reflecting the asymmetric orbital occupancies due to the selection rules of dipole transitions. As shown in Fig. 6(*a*), the main spectral features of the polar and nonpolar lattices are marked A–E. The two peaks A and B with low photon energies are dominated by O 2*p* states hybridized with Zn 4*s* orbital levels. Peaks C and D can be assigned to O 2*p* hybridized with Zn 4*p* states. Our previous reports have demonstrated that the partial density of states of oxygen p_z and $p_x(p_y)$ orbitals are separated at about 12 eV and 15 eV above the Fermi level for ZnO systems, which directly correspond to the peaks C and D resolved in the O *K*-edge XAS spectra, respectively. The broad multiplet excitation peaks labeled E with photon energies >550 eV can be attributed to the O 2*p* and Zn 4*d* hybridized states. The assignments of these characteristic peaks are the same as that proposed for ZnO single crystals, ZnO films and the band structure calculations therein (Vaithianathan *et al.*, 2009; Li *et al.*, 2016; Mosquera *et al.*, 2013).

Fig. 6(*a*) shows the angular-dependent O *K*-edge XAS spectra for pristine and N-doped nonpolar *m*-plane ZnO samples. Firstly, a negligible angular-dependent spectral variation is observed for both pristine (dotted lines) and N-doped (solid lines) *m*-plane ZnO, which indicates comparable orbital occupations of O p_z and $p_x(p_y)$ orbitals. Secondly, a slight reduction in intensity of peak C denoting the O $2p_z$–Zn *4p* hybridized state and a hint of enhanced intensity of peak D denoting the O $2p_x(p_y)$–Zn 4*p* hybridized state are observed upon nitrogen incorporation, which might be related to the structural distortions due to the increased amount of oxygen vacancies and the different ionic radius of N in replacement of O. Fig. 6(*b*) shows the angular-dependent O *K*-edge XAS spectra of *o*-plane ZnO samples before and after nitrogen doping. Both pristine and doped lattices show an obvious angular dependence. The XAS spectra with normal incident angle $\theta = 90°$ are comparable with the spectral features observed for *m*-plane ZnO. However, as θ decreases from 90° to 30°, the relative peak intensity of A increases. Peak A has been demonstrated with a stronger sensitivity to surface states where variation of the peak intensity can be used to evaluate the surface relaxation phenomena as suggested by the compared XAS spectra collected with surface-sensitive TEY and bulk-sensitive total fluorescence yield modes (Chiou *et al.*, 2004). The enhanced peak A intensity with $\theta = 30°$ suggests that more surface states exist with σ-character in *o*-plane ZnO compared with *m*-plane ZnO lattices, which is consistent with the assignment of peak A as the σ-type interaction between Zn and O atoms in the literature. Moreover, as θ decreases, peak C shows an increased peak intensity whereas peak D undergoes a contrary trend. The charge redistributions at peaks C and D suggest increased unoccupied p_z orbitals and a decreased unoccupied state with $p_x(p_y)$ symmetry as θ decreases. The existence of more unoccupied $2p_z$ orbitals implies more electrons occupied the $2p_x(p_y)$ orbitals, which might be caused by the reduction of symmetry of the surface layers due to surface reconstruction and oxygen vacancies formed by ion bombardments and lattice relaxations, *etc.* (Cho *et al.*, 2009; Dong *et al.*, 2004). Our results suggest different electronic structures and surface states for polar and nonpolar ZnO lattices. Angular-dependent O *K*-edge XAS can thus be used as an effective method to monitor the surface physics in ZnO systems.

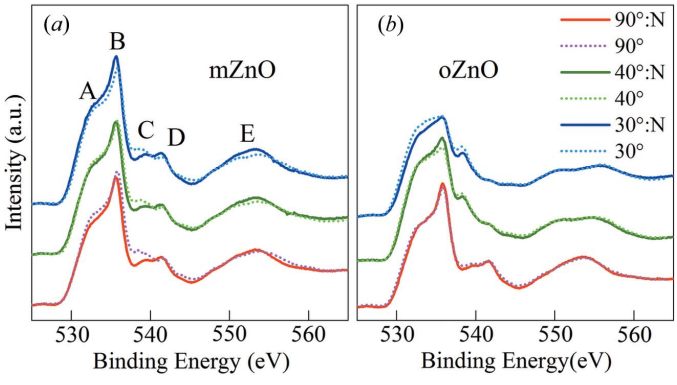

Figure 6
Angular-dependent O *K*-edge XAS spectra of (*a*) N-doped *m*-plane (solid lines) ZnO and the pristine *m*-ZnO (dotted lines) and (*b*) N-doped *o*-plane ZnO (solid lines) and the pristine *o*-ZnO (dotted lines) with incident angles $\theta = 90°$, 40° and 30°.

4. Conclusions

We performed detailed electronic structure studies on nitrogen-incorporated ZnO lattices with both $(000\bar{1})$-terminated polar *o*-plane and $(10\bar{1}0)$-terminated nonpolar *m*-plane ZnO surfaces. The investigated ZnO lattices show the desired crystal orientations as confirmed by LEED measurements. *In situ* XPS measurements were performed to determine the chemical bonding information after nitrogen incorporation. The N-doped samples show characteristic N—Zn and N—O chemical bonds indicating the successful incorporation of N ions in ZnO lattices. Moreover, the stronger N—Zn peak intensity observed in the *o*-plane compared with the *m*-plane ZnO suggests a more favorable chemical environment for the efficient doping of N elements in the *o*-plane ZnO lattices, which is consistent with the lower formation energy for N substituting Zn in the O-rich surface as suggested by first-principle calculations (Wang *et al.*, 2016). The variations of the electronic states near the Fermi level have been investigated through combined UPS and O *K*-edge XAS measurements. Energy shifts of the VBM towards the Fermi level have been resolved for both polar and nonpolar ZnO lattices whereas a charge redistribution of the O 2*p* hybridized states is only resolved from *o*-plane ZnO with a polar surface. No significant modification of the O *K*-edge XAS reflecting the conduction band minimum near the Fermi level has been observed between pristine ZnO and N-doped ZnO samples. However, the *o*-plane ZnO lattices show strong angular-dependent XAS features, indicating that more surface states are involved in

determining the physical and chemical properties in polar ZnO. Moreover, the angular dependence of the multiplet structure in *o*-plane ZnO suggests an asymmetric occupation of the O 2*p* orbital which might be related to the lowering of crystal symmetry due to structural variation of the surface layers. These observations strongly suggest that crystallographic polarity is a highly influential factor in controlling the band structure and properties in ZnO systems. Our results provide a possible underlying mechanism for the different influence of nitrogen doping between polar and nonpolar ZnO lattices as well as the modification of the electronic structures toward p-type doping of ZnO compounds. The distinct electronic structure resolved for polar and nonpolar ZnO lattices may also offer guidance for the material design of other systems utilizing polar and nonpolar interfaces.

Funding information

We acknowledge the financial support by the National Natural Science foundation of China (grant No. 11704317), the China Postdoctoral Science Foundation (grant No. 2016M602064), the Natural Science Foundation of Fujian Province (grant No. 2017J01013), the Fundamental Research Funds for Central Universities (grant No. 20720160020) and Xiamen University Malaysia Research Fund (grant No. XMUMRF/2019-C4/IORI/0002).

References

Allen, M. W., Mendelsberg, R. J., Reeves, R. J. & Durbin, S. M. (2009). *Appl. Phys. Lett.* **94**, 103508.
Bian, J. M., Li, X. M., Gao, X. D., Yu, W. D. & Chen, L. D. (2004). *Appl. Phys. Lett.* **84**, 541–543.
Brillson, L. J., Zhang, Z., Doutt, D. R., Look, D. C., Svensson, B. G., Kuznetsov, A. Y. & Tuomisto, F. (2013). *Phys. Status Solidi*, **250**, 2110–2113.
Chang, Q. S. (2004). *Phys. Rev. B Condens. Matter*, **69**, 1129–1133.
Chen, J. G. (2010). *ChemInform*, **29**, 1–152.
Chen, M., Wang, X., Yu, Y. H., Pei, Z. L., Bai, X. D., Sun, C., Huang, R. F. & Wen, L. S. (2000). *Appl. Surf. Sci.* **158**, 134–140.
Chiou, J. W., Jan, J. C., Tsai, H. M., Bao, C. W., Pong, W. F., Tsai, M. H., Hong, I. H., Klauser, R., Lee, J. F., Wu, J. J. & Liu, S. C. (2004). *Appl. Phys. Lett.* **84**, 3462–3464.
Cho, D. Y., Kim, J. H., Na, K. D., Song, J., Hwang, C. S., Park, B., Kim, J., Min, C. & Oh, S. (2009). *Appl. Phys. Lett.* **95**, 261903.
Dong, C. L., Persson, C., Vayssieres, L., Augustsson, A., Schmitt, T., Mattesini, M., Ahuja, R., Chang, C. L. & Guo, J. H. (2004). *Phys. Rev. B*, **70**, 3352–3359.
Fan, J. C., Sreekanth, K. M., Xie, Z., Chang, S. L. & Rao, K. V. (2013). *Prog. Mater. Sci.* **58**, 874–985.
Gao, Y. K., Traeger, F., Shekhah, O., Idriss, H. & Wöll, C. (2009). *J. Colloid Interface Sci.* **338**, 16–21.
Gasset, M., Oñaderra, M., Goormaghtigh, E. & Gavilanes, J. G. (1991). *Biochim. Biophys. Acta*, **1080**, 51–58.
Ghosh, B., Ray, S. C., Pontsho, M., Sarma, S., Mishra, D. K., Wang, Y. F., Pong, W. F. & Strydom, A. M. (2018). *J. Appl. Phys.* **123**, 161507.
Guan, H., Xia, X., Zhang, Y., Gao, F., Li, W., Wu, G., Li, X. & Du, G. (2008). *J. Phys. Condens. Matter*, **20**, 292202.
Janotti, A. & Van de Walle, C. G. (2009). *Rep. Prog. Phys.* **72**, 126501.
Jedrecy, N., Gallini, S., Sauvage-Simkin, M. & Pinchaux, R. (2000). *Surf. Sci.* **460**, 136–143.
Kim, T., Yoshitake, M., Yagyu, S., Nemsak, S., Nagata, T. & Chikyow, T. (2010). *Surf. Interface Anal.* **42**, 1528–1531.
Lafrentz, M., Brunne, D., Rodina, A. V., Pavlov, V. V., Pisarev, R. V., Yakovlev, D. R., Bakin, A. & Bayer, M. (2013). *Phys. Rev. B*, **88**, 6100–6105.
Lashkarev, G. V., Shtepliuk, I. I., Ievtushenko, A. I., Khyzhun, O. Y., Kartuzov, V. V., Ovsiannikova, L. I., Karpyna, V. A., Myroniuk, D. V., Khomyak, V. V., Tkach, V. M., Timofeeva, I. I., Popovich, V. I., Dranchuk, N. V., Khranovskyy, V. D. & Demydiuk, P. V. (2015). *Low Temp. Phys.* **41**, 129–140.
Li, D., Wang, H., Zhou, H., Li, Y., Huang, Z., Zheng, J., Wang, J., Qian, H., Ibrahim, K. & Chen, X. (2016). *Chin. Phys. B*, **25**, 331–335.
Li, L. K., Jurkovic, M. J., Wang, W. I., Van Hove, J. M. & Chow, P. P. (2000). *Appl. Phys. Lett.* **76**, 1740–1742.
Lin, Y. J. & Tsai, C. L. (2006). *J. Appl. Phys.* **100**, 173503.
Maki, H., Sakaguchi, I., Ohashi, N., Sekiguchi, S., Haneda, H., Tanaka, J. & Ichinose, N. (2003). *Jpn. J. Appl. Phys.* **42**, 75–77.
Mosquera, A. A., Horwat, D., Rashkovskiy, A., Kovalev, A., Miska, P., Wainstein, D., Albella, J. M. & Endrino, J. L. (2013). *Sci. Rep.* **3**, 357–360.
Nickel, N. H. & Terukov, E. (2005). *Zinc Oxide – A Material for Micro- and Optoelectronic Applications*, Part of the *NATO Science Series II: Mathematics, Physics and Chemistry Book Series*, Vol. 194. Dordrecht: Springer Netherlands.
Ogale, S. B. (2005). Editor. *Multifunctional Thin Film.* Boston: Springer.
Özgür, Ü., Alivov, Y. I., Liu, C., Teke, A., Reshchikov, M. A., Doğan, S., Avrutin, V., Cho, S. J. & Morkoç, H. (2005). *J. Appl. Phys.* **98**, 11.
Park, S. M., Ikegami, T. & Ebihara, K. (2006). *Thin Solid Films*, **513**, 90–94.
Perkins, C. L., Lee, S. H., Li, X., Asher, S. E. & Coutts, T. J. (2005). *J. Appl. Phys.* **97**, 155334.
Petravic, M., Deenapanray, P. N. K., Coleman, V. A., Jagadish, C., Kim, K. J., Kim, B., Koike, K., Sasa, S., Inoue, M. & Yano, M. (2006). *Surf. Sci.* **600**, L81–L85.
Rochet, F. (1998). *J. Vac. Sci. Technol. B*, **16**, 1692–1696.
Schwarz, W. H. E., Chang, T. C. & Connerade, J. P. (1977). *Chem. Phys. Lett.* **49**, 207–212.
Seah, M. P. & Dench, W. A. (1979). *Surf. Interface Anal.* **1**, 2–11.
Shinde, S. S., Shinde, P. S., Oh, Y. W., Haranath, D., Bhosale, C. H. & Rajpure, K. Y. (2012). *J. Anal. Appl. Pyrolysis*, **97**, 181–188.
Sun, C. Q., Li, C. M., Li, S. & Tay, B. K. (2004). *Phys. Rev. B*, **69**, 1681–1685.
Tabet, N., Faiz, M. & Al-Oteibi, A. (2008). *J. Electron Spectrosc. Relat. Phenom.* **163**, 15–18.
Vaithianathan, V., Asokan, K., Park, J. Y. & Kim, S. S. (2009). *Appl. Phys. A*, **94**, 995–998.
Wang, H., Zhan, H., Zhou, Y., Wu, Y., Chen, X., Wang, H. & Kang, J. (2016). *Nanoscale* **8**, 4381–4386.
Wang, X., Tomita, Y., Roh, O. H., Ohsugi, M. & Yoshikawa, A. (2005). *Appl. Phys. Lett.* **86**, 383.
Wei, H., Wu, Y., Wu, L. & Hu, C. (2005). *Mater. Lett.* **59**, 271–275.
Wight, G. R. & Brion, C. E. (1974). *J. Electron Spectrosc. Relat. Phenom.* **4**, 25–42.
Williams, J. R., Kobata, M., Pis, I., Ikenaga, E., Sugiyama, T., Kobayashi, K. & Ohashi, N. (2011). *Surf. Sci.* **605**, 1336–1340.
Yang, A. L., Song, H. P., Wei, H. Y., Liu, X. L. & Wang, Z. G. (2009). *Appl. Phys. Lett.* **94**, 115.
Yeh, J. J. & Lindau, I. (1985). *At. Data Nucl. Data Tables*, **32**, 1–155.
Zhang, Y., Lin, N., Li, Y., Wang, X., Wang, H., Kang, J., Wilks, R., Bär, M. & Mu, R. (2016). *Sci. Rep.* **6**, 23106.
Zhou, H., Wang, H. Q., Liao, X. X., Zhang, Y., Zheng, J. C., Wang, J. O., Muhemmed, E., Qian, H. J., Ibrahim, K. & Chen, X. (2012). *Nanoscale Res. Lett.* **7**, 184.